

# Radio-Interferometric Image Reconstruction with Denoising Diffusion Restoration Models

M. Morales,<sup>1</sup> E. Tolley,<sup>1\*</sup> R. Poitevineau<sup>1</sup>

<sup>1</sup> *Institute of Physics, Laboratory of Astrophysics, École Polytechnique Fédérale de Lausanne (EPFL), 1290 Sauverny, Switzerland*

Accepted XXX. Received YYY; in original form ZZZ

## ABSTRACT

Reconstructing images of the radio sky from incomplete Fourier information is a key challenge in radio astronomy. In this work, we present a method for radio interferometric image reconstruction using a data-driven prior for the radio sky based on denoising diffusion probabilistic models (DDPMs). We train a DDPM on radio galaxy observations from the VLA FIRST survey, then create simulated VLA, EHT, and ALMA observations of radio galaxies. We use an unsupervised posterior sampling method called Denoising Diffusion Restoration Models (DDRM) to reconstruct the corresponding images using our DDPM as a prior. Our approach is agnostic to the measured radio interferometric data and naturally incorporates the physics of the measurement process. We are able to reconstruct images with very high fidelity and demonstrate a marked improvement over image reconstruction techniques that work on gridded visibilities like CLEAN.

**Key words:** Machine Learning – Image Synthesis – Radio Galaxies

## 1 INTRODUCTION

The sparse layouts of radio interferometers result in an incomplete sampling of the sky in Fourier space. Aperture synthesis by radio interferometry aims to reconstruct images of the radio sky from this incomplete Fourier information. This ill-posed inverse problem requires advanced image formation algorithms and strong regularization to compensate for the missing information.

Traditional imaging in radio-interferometry has relied on the CLEAN algorithm introduced in Högbom (1974), a sparse matching pursuit algorithm. CLEAN has had many variants and improvements over the decades, such as Multi-scale CLEAN (Cornwell 2008), W-projection, W-stacking, w-snapshotting techniques (Cornwell et al. 2008; Cornwell & Perley 1992; Ord et al. 2010), which correct the non-coplanar baseline term, A-projection (Bhatnagar et al. 2008) that correct per antenna gain variation. These improvements have made CLEAN a robust algorithm that is a staple of radio-interferometric imaging. Despite CLEAN’s success it still has certain limitations. The performance relies on user-defined parameters, the imaging lacks uncertainty quantification, and complex emission can be difficult to model with CLEAN’s discrete components.

Computational imaging techniques provide an alternate approach to image reconstruction. These methods model how the observations  $y$  depend on the sky model  $x$ , use additional regularization terms such as sparsity priors. These techniques include maximum entropy methods (MEM; Ponsonby 1973; Ables 1974; Cornwell & Evans 1985; Narayan & Nityananda 1986), compressed sensing (CS) and sparse reconstruction methods (for example, Wiaux et al. 2009; Li et al. 2011; Carrillo et al. 2012; Dabbech et al. 2015; Terris et al. 2023), and regularized maximum likelihood imaging (RML; The Event Horizon Telescope Collaboration 2019; Zawadzki et al. 2023).

Recent machine learning approaches in radio-interferometric imaging also show promising results, learning the distribution of the radio sky rather than relying on a hand-crafted prior. Gheller & Vazza (2022) and Connor et al. (2022) developed neural networks which learn the mapping between the dirty image and the true radio sky. Schmidt et al. (2022) redefined the deconvolution problem as inpainting in Fourier space, using a residual neural network (He et al. 2016). Aghabiglou et al. (2024) developed a series of Deep Neural Networks (DNNs) and formulate reconstruction as a series of images, with each DNN taking the previous iteration’s image estimate and associated data residual as inputs. Drozdova et al. (2024) and Wang et al. (2023) developed conditional Denoising Diffusion Probabilistic Models (DDPM; Ho et al. 2020) to deconvolve dirty images.

However, all of these machine learning methods rely on learning a specific antenna configuration. These networks must be retrained to apply to different telescopes, or even to use for observations with different observing times or pointing directions.

In this paper we present a deep learning method for interferometric image reconstruction that does not need to be trained on any specific antenna configuration, as it naturally incorporates the physics of the measurement process. First, we train a DDPM which learns the morphology of radio galaxies from VLA FIRST (Becker et al. 1995) survey which serves as a data-driven prior. Then we implement image reconstruction method using a chain of conditional reconstruction steps called Denoising Diffusion Restoration (DDRM; Kwar et al. 2022) to obtain samples consistent both with the noisy observation and with the distribution of training data. We evaluate our results on using a simplified reconstruction pipeline of the VLA array layout, and compare the performance to CLEAN, WSCLEAN, and an implementation of the MORESANE compressed sensing algorithm.

The paper is organized as follows. Section 2 covers our methodology, including a formulation of image reconstruction as an inverse problem, an introduction to DDPMs and DDRM sampling, an

\* E-mail: emma.tolley@epfl.ch

overview of the data used for training and validation, and our process for creating our mock observations. Results are presented in 3, including comparisons to other deconvolution methods, tests with variable noise levels, and imaging out-of-domain data.

## 2 METHODS

### 2.1 Aperture synthesis in radio interferometry

A radio interferometer measures the spatial coherence function of the electric fields measured at antenna positions  $\vec{r}_p$  and  $\vec{r}_q$  (Cornwell et al. 2008):

$$V_{pq} = \langle E(\vec{r}_p, t) E(\vec{r}_q, t)^* \rangle_t, \quad (1)$$

These measurements, usually called visibilities, are often expressed as  $V(u, v, w)$ , where  $u, v, w$  are components of the vector between the two interferometer elements expressed in units of wavelength of the radiation. The visibilities can be related to the sky brightness distribution  $I(l, m)$  via the van Cittert-Zernike theorem (Ostrovsky et al. 2009):

$$V(u, v, w) = \iint I(l, m) e^{-2\pi i[ul+vm+wn]} \frac{dl dm}{n+1} + z(u, v, w), \quad (2)$$

where  $n := \sqrt{1 - l^2 - m^2} - 1$  and  $\eta$  are Gaussian-distributed uncorrelated noise terms. In the small-field approximation where  $n \approx 0$ , we can rewrite this in matrix notation (Thyagarajan et al. 2017) as:

$$\mathbf{y} = \mathbf{S}\mathcal{F}\mathbf{x} + \mathbf{z}, \quad (3)$$

where the visibilities  $\mathbf{y} \in \mathbb{C}^m$  for  $m$  antenna pairs,  $\mathbf{x} \in \mathbb{R}^n$  is the flattened radio sky image,  $\mathcal{F} \in \mathbb{C}^{n \times n}$  is the 2D Fourier transform matrix,  $\mathbf{S} \in \mathbb{C}^{m \times n}$  is the sampling matrix due to the finite number of antennas, and  $\mathbf{z} \in \mathbb{R}^m$  are uncorrelated noise terms. We note that the sampling matrix  $\mathbf{S}$  depends on the interferometer layout and observation configuration.

CLEAN starts by reconstructing an initial estimate of  $\mathbf{x}$  through back-projection, called the ‘‘dirty image’’:

$$\mathbf{x}_D = \mathcal{F}^{-1}\mathbf{y} = \mathcal{F}^{-1}(\mathbf{S}) * \mathbf{x} + \mathcal{F}^{-1}\mathbf{z}, \quad (4)$$

and the ‘‘dirty beam’’  $\mathcal{F}^{-1}(\mathbf{S})$  is iteratively removed from the dirty image  $\mathbf{x}_D$  by populating a model of the radio sky with discrete components. Hogbom CLEAN (Högbom 1974) uses point sources as its components, whereas Multi-Scale (MS) CLEAN (Cornwell 2008; Rich et al. 2008) uses point and extended sources modeled with a tapered quadratic function. Both variations of CLEAN are *matching pursuit* algorithms that approximately maximize the posterior with an implicit sparsity prior Bergeaud & Mallat (1995). The compressed sensing algorithm MORESANE (Dabbech et al. 2015) adds components across multiple scales using the Isotropic Undecimated Wavelet Transform (IUWT Starck et al. 2007).

### 2.2 Denoising Diffusion Probabilistic Models

For more details about DDPM, its theoretical foundation, capabilities, and training algorithms we refer the reader to Ho et al. (2020). The DDPM process is defined by two Markov chains, a forward (diffusion) and backwards (denoising) process. The forward process  $q(\mathbf{x}_{1:T}|\mathbf{x}_0)$  gradually adds Gaussian noise to the original data  $\mathbf{x}_0$  over  $T$  steps, producing a sequence of increasingly noisy samples  $\mathbf{x}_1, \dots, \mathbf{x}_T$ :

$$q(\mathbf{x}_{1:T}|\mathbf{x}_0) := \prod_{t=1}^T q(\mathbf{x}_t|\mathbf{x}_{t-1}). \quad (5)$$

Each transition  $q(\mathbf{x}_t|\mathbf{x}_{t-1})$  adds noise which takes the form of a Gaussian distribution with decreasing signal-to-noise ratio determined by the schedule  $\beta_t$ :

$$q(\mathbf{x}_t|\mathbf{x}_{t-1}) := \mathcal{N}(\mathbf{x}_t; \sqrt{1 - \beta_t}\mathbf{x}_{t-1}, \beta_t\mathbf{I}). \quad (6)$$

The reverse process  $p_\theta(\mathbf{x}_{0:T})$  is learned by a neural network to approximate the reverse of the forward diffusion:

$$p_\theta(\mathbf{x}_{0:T}) := p(\mathbf{x}_T) \prod_{t=1}^T p_\theta(\mathbf{x}_t|\mathbf{x}_{t+1}), \quad (7)$$

where  $\theta$  refers to the parameters of the neural network. This Markov chain starts from a sample  $\mathbf{x}_T \sim \mathcal{N}(0, \mathbf{I})$  and attempts to remove a small amount of Gaussian noise at each step. The step function is modeled with:

$$p_\theta(\mathbf{x}_t|\mathbf{x}_{t+1}) := \mathcal{N}(\mathbf{x}_t; f_\theta(\mathbf{x}_{t+1}, t), \sigma_t^2\mathbf{I}) \quad (8)$$

where the mean function  $f_\theta(\mathbf{x}_{t+1}, t)$  is the output of the neural network and  $\sigma_t^2$  is the accumulated variance noise at each timestep  $t$ . The operation is repeated  $T$  times to recover the denoised sample  $\hat{\mathbf{x}}_0$ .

#### 2.2.1 Network Architecture

We implement a DDPM using the U-Net architecture (Ronneberger et al. 2015), a multi-scale convolutional neural network with skip-connections to preserve fine detail. The network has two parts, an encoder that progressively compresses the image to higher-level features, and a decoder that progressively reconstructs the image from these features. Each encoder and decoder block is made up of two Resnet (He et al. 2016) blocks with FiLM layers (Perez et al. 2017) after each LayerNorm (Lei Ba et al. 2016). The network has a total of 40 million free parameters. A diagram of the network architecture is shown in Figure 1.

### 2.3 Denoising Diffusion Restoration models for radio-interferometry

Kawar et al. (2022) introduced the diffusion restoration model (DDRM), which defines a Markov chain conditioned on observations  $\mathbf{y}$  which performs approximate posterior sampling for  $p(\mathbf{x}_0|\mathbf{y})$ , where the prior on the true image  $p(\mathbf{x}_0)$  is implicitly given by a pretrained diffusion model. DDRM samples from a constrained generative process:

$$p_\theta(\mathbf{x}_{0:T}|\mathbf{y}) := p(\mathbf{x}_T|\mathbf{y}) \prod_{t=1}^T p_\theta(\mathbf{x}_{t-1}|\mathbf{x}_t, \mathbf{y}). \quad (9)$$

The measurements  $\mathbf{y}$  are obtained from the true image  $\mathbf{x}$  from a linear forward model:

$$\mathbf{y} = \mathbf{H}\mathbf{x} + \mathbf{z}, \quad (10)$$

where  $\mathbf{H}$  is the linear transformation operator and  $\mathbf{z}$  is zero-mean Gaussian noise with variance  $\sigma_y^2$ . Their solution is expressed in the singular space of the sampling operator and therefore starts with computing its singular value decomposition (SVD):

$$\mathbf{H} = \mathbf{U}\mathbf{\Sigma}\mathbf{V}^\top, \quad (11)$$

then applying the transformations  $\bar{\mathbf{y}} := \mathbf{\Sigma}^+\mathbf{U}^\top\mathbf{y}$  (where  $\mathbf{\Sigma}^+$  is a Moore–Penrose pseudo-inverse) and  $\bar{\mathbf{x}} := \mathbf{V}^\top\mathbf{x}$ . If  $f_\theta(\mathbf{x}_{t+1}, t)$  is the prediction made by the DDPM model at timestep  $t + 1$ , we define  $\bar{\mathbf{x}}_{\theta,t} := \mathbf{V}^\top f_\theta(\mathbf{x}_{t+1}, t)$ . The sampling procedure then considers separately components according to the singular values of the transformation operator.

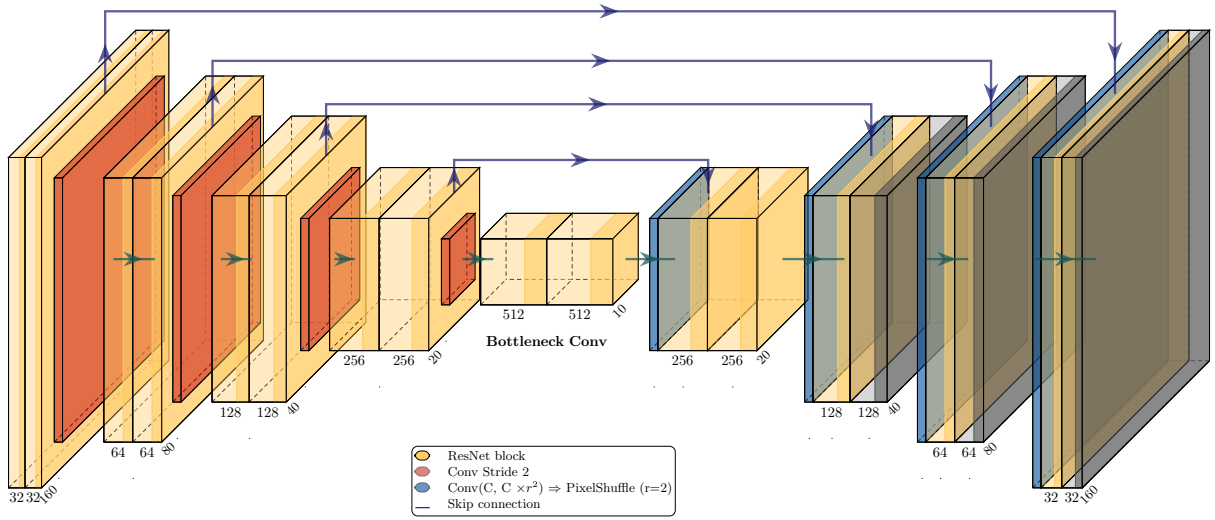


Figure 1. Neural Network Architecture used for the DDPM network.

For components with zero singular value ( $s_i = 0$ ), we have no information from the measurements  $\mathbf{y}$  and sample according to the prior only:

$$p_{\theta}(\bar{\mathbf{x}}_t^{(i)} | \mathbf{x}_{t+1}, \mathbf{y}) = \mathcal{N}\left(\bar{\mathbf{x}}_{\theta,t}^{(i)} + \sqrt{1 - \eta^2} \sigma_t \frac{\bar{\mathbf{x}}_{t+1}^{(i)} - \bar{\mathbf{x}}_{\theta,t}^{(i)}}{\sigma_{t+1}}, \eta^2 \sigma_t^2\right). \quad (12)$$

When measurement is uncertain ( $\sigma_t < \sigma_y/s_i$ ), the update is guided by the measurement and weighted based on the uncertainty:

$$p_{\theta}(\bar{\mathbf{x}}_t^{(i)} | \mathbf{x}_{t+1}, \mathbf{y}) = \mathcal{N}\left(\bar{\mathbf{x}}_{\theta,t}^{(i)} + \sqrt{1 - \eta^2} \sigma_t \frac{\bar{\mathbf{y}}^{(i)} - \bar{\mathbf{x}}_{\theta,t}^{(i)}}{\sigma_y/s_i}, \eta^2 \sigma_t^2\right). \quad (13)$$

When the measurement is certain compared to the prior's variance schedule ( $\sigma_t \geq \sigma_y/s_i$ ), the variance shrinks accordingly:

$$p_{\theta}(\bar{\mathbf{x}}_t^{(i)} | \mathbf{x}_{t+1}, \mathbf{y}) = \mathcal{N}\left((1 - \eta_b)\bar{\mathbf{x}}_{\theta,t}^{(i)} + \eta_b\bar{\mathbf{y}}^{(i)}, \sigma_t^2 - \frac{\sigma_y^2}{s_i^2} \eta_b^2\right) \quad (14)$$

In all three cases  $\eta$  and  $\eta_b$  are hyperparameters that respectively control the amount of stochastic noise injected during sampling and the strength with which the measurement is enforced in the reverse process. In this work we use  $\eta = 0.85$  and  $\eta_b = 1.0$ , following (Kawar et al. 2022). When setting  $\eta_b = 1.0$ , the sampling procedure will exclusively update using the observation  $\mathbf{y}$  if the measurement noise is smaller than the variance schedule weighted by the singular value.

To adapt the forward model in equation 10 and corresponding SVD for aperture synthesis, we define the transformation operator  $\mathbf{H} = \mathbf{S}\mathcal{F}$ . We first find a memory-efficient SVD of  $\mathbf{S}$  following the method presented in Kawar et al. (2022):

$$\mathbf{S} = \mathbf{I}\mathbf{K}\mathbf{P}, \quad (15)$$

where  $\mathbf{P}$  is an appropriate permutation matrix,  $\mathbf{K}$  is a rectangular diagonal matrix of size  $m \times n$  with the gridded visibility weights in its main diagonal, and  $\mathbf{I}$  is the identity matrix. Because  $\mathcal{F}$  is unitary, we can easily define the complex SVD:  $\mathbf{H} = \mathbf{U}\mathbf{\Sigma}\mathbf{V}^*$ , where  $\mathbf{U} = \mathbf{I}$ ,  $\mathbf{\Sigma} = \mathbf{K}$ , and  $\mathbf{V}^* = \mathbf{P}\mathcal{F}$ , with  $\mathbf{V} = \mathcal{F}^{-1}\mathbf{P}^T$ . This accurately represents the radio astronomy measurement equation in the small-field approximation, but does not include the effect of  $w$ -terms or  $A$ -terms. Instead of

calculating the Fourier matrixes directly, we implement them with the pytorch implementation of the fast fourier transform FFT2.

The general computational complexity of our method is  $\mathcal{O}(K \cdot (C(N) + S(N)))$ , where  $K$  is the number of sampling steps,  $C(N)$  and  $S(N)$  are the complexity of the neural network and the measurement consistency step, with respect to the number of pixels  $N$ . In our neural network, our complexity is  $C(N) = \mathcal{O}(N)$  and our data consistency step complexity is dominated by the FFT2 algorithm, hence  $S(N) = \mathcal{O}(N \cdot \log(N))$ . Therefore the total complexity of the our method is  $\mathcal{O}(K \cdot N \cdot \log(N))$ .

## 2.4 Data & Training

Before using DDRM, we first need to train our DDPM model which serves as the data-driven prior. For this we used two different overlapping radio galaxy datasets. The first is a collection and combination of several catalogues using the VLA FIRST (Faint Images of the Radio Sky at Twenty-Centimeters) survey (Becker et al. 1995), curated by Griese et al. (2023). It contains galaxies identified as FRI, FRII, compact, or bent sources. We also use 20k FIRST radio galaxies from the Radio Galay Zoo DR1 (Wong et al. 2025). These datasets contain images of radio galaxies of size  $150 \times 150$  pixels and  $300 \times 300$  pixels, respectively, and are flux-normalized to the range  $[0,1]$ . We crop the larger images to  $150 \times 150$  for consistency between the two datasets. This sample of radio galaxies comprise the set of our true images  $\{\mathbf{x}\}$ . We use 200 images for validation data, 200 for test data, and 21,758 images for training following the validation and test split of Griese et al. (2023). A selection of radio galaxies from the test dataset are shown in Figure 2.

For training the model, we use data augmentation, including random shifts with a maximum distance of 20 pixels, random rotation, vertical and horizontal flips, as well as multiplying each pixel in the image by a single randomly chosen value between 0.8 and 1.2, then clipped back to  $[0, 1]$  before being mapped to  $[-1,1]$  for DDPM training or DDRM sampling.

We train our 40-million parameter DDPM neural network for 300'000 optimizer steps, using the DDPM training algorithm described in Ho et al. (2020). We use PyTorch's AdamW (Loshchilov & Hutter 2017) with  $\beta_1 = 0.9$  and  $\beta_2 = 0.999$  and weight decay  $1 \times 10^{-2}$ . The learning rate follows a linear schedule from optimizer

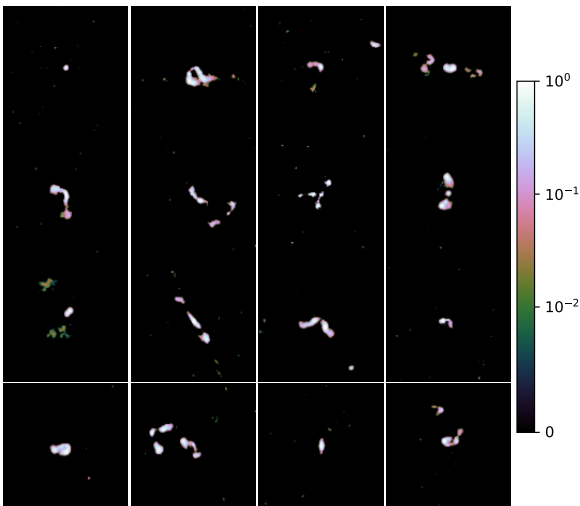


Figure 2. A selection of radio galaxies from the test dataset.

step 0 to 15'000, going from  $2 \times 10^{-7}$  to  $2 \times 10^{-4}$ , then we use a cosine annealing schedule (Loshchilov & Hutter 2016). The model was compiled using `torch.compile` with the `inductor` backend in `max-autotune` mode with static shapes (`dynamic=False`). This gives us a model that is able to generate images from our training dataset unconditionally, starting from Gaussian noise.

As an additional test image, we use an image of the radio galaxy 3c535 from Terris et al. (2023). We create several  $150 \times 150$  pixel cutouts of this radio galaxy through cropping and resampling.

## 2.5 Experimental Setup

To define a realistic sampling matrix  $\mathbf{S}$  we use three different telescope configurations:

(i) **VLA**: We use a simulation of the Very Long Array (VLA) for 60 time steps, representing approximately 2 hours of observation time, implemented with the radio interferometer observation simulation tool from the RadioNets library (Schmidt et al. 2022).

(ii) **EHT**: We use a sampling matrix representing the  $(u, v)$  coverage the Event Horizon Telescope (EHT; Event Horizon Telescope Collaboration 2019) telescope from Wang et al. (2023), resized to match our  $150 \times 150$  pixel input data.

(iii) **ALMA**: We use a sampling matrix representing the  $(u, v)$  coverage the Atacama Large Millimeter Array (ALMA) from Taran et al. (2023) resized to match our  $150 \times 150$  pixel input data.

We construct the visibilities  $\mathbf{y}$  and dirty images following Eq. 4. The sampling matrix  $\mathbf{S}$ , dirty beam  $\mathcal{F}^{-1}\mathbf{S}$ , and example dirty image  $\mathbf{x}_D = \mathcal{F}^{-1}(\mathbf{S}) * \mathbf{x}$  is shown for VLA, ALMA, and EHT in Figure 3. Most results in this work show image reconstruction results for an  $\mathbf{S}$  that corresponds uniform UV weights, but show additional tests with natural weights in Appendices A and B.

We also add  $\sigma_y$  noise to the dirty images. As the input sky image  $\mathbf{x}$  is always scaled from  $[0,1]$ , the noise added is defined as a fraction of the maximum flux of the image.

Once we have our measurement  $\mathbf{y} = \mathcal{F}\mathbf{x}_D$ , we then run the DDRM sampling algorithm using our trained DDPM model following the methodology described in Section 2.3 to reconstruct a clean image of the radio sky.

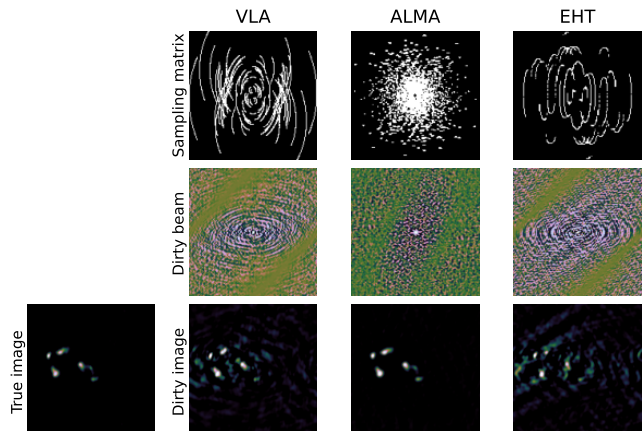


Figure 3. Diagram of the sampling matrix  $\mathbf{S}$ , dirty beam  $\mathcal{F}^{-1}\mathbf{S}$ , true image  $\mathbf{x}$ , dirty image  $\mathbf{x}_D = \mathcal{F}^{-1}(\mathbf{S}) * \mathbf{x}$  for the three telescopes considered in this work.

## 2.6 Metrics

We use three metrics for evaluating the quality of the results. The first is Mean Squared Error (MSE), defined as:

$$\text{MSE} = \frac{1}{NM} \sum_{i=1}^N \sum_{j=1}^M (\mathbf{x}^{(j)} - \hat{\mathbf{x}}_i^{(j)})^2, \quad (16)$$

where  $\mathbf{x}$  is our true image,  $\hat{\mathbf{x}}_i$  is our  $i$ th prediction, and  $j$  indexes the  $M$  pixels of the image. We also report the peak signal-to-noise ratio (PSNR) for comparison to other methods, defined as:

$$\text{PSNR} = 10 \times \log_{10} \left( \frac{\text{MAX}}{\text{MSE}} \right), \quad (17)$$

where  $\text{MAX} = 1$  for all images in our dataset, and the signal-to-noise ratio (SNR) defined as:

$$\text{SNR} = 10 \times \log_{10} \left( \frac{\frac{1}{N} \sum_j \mathbf{x}^{(j)}}{\text{MSE}} \right) \quad (18)$$

Finally, we evaluate the standardised reconstruction error (SRE), by measuring the reconstruction error relative to the reconstruction variability:

$$\text{SRE} = \frac{1}{NM} \sum_{i=1}^N \sum_{j=1}^M \frac{|\hat{\mathbf{x}}_i^{(j)} - \mathbf{x}^{(j)}|}{\sigma^{(j)}} \quad (19)$$

where  $\sigma^{(j)}$  is the per-pixel standard deviation map:

$$\sigma^{(j)} = \sqrt{\mathbb{E} \left[ (\hat{\mathbf{x}}^{(j)} - \mathbb{E}[\hat{\mathbf{x}}^{(j)}])^2 \right]}. \quad (20)$$

Like MSE, the SRE penalizes large errors in solution, but also takes into account if the predicted solution is within the empirical reconstruction variability.

## 3 RESULTS

After training our DDPM on the training data, we evaluate the DDRM reconstruction on the reserved test data. The results of our image reconstruction with DDRM are shown in Figure 4, for our simulated VLA observation with no added noise. DDRM is able to reconstruct the central morphology of the sources with impressive accuracy and no remaining dirty beam artifacts.

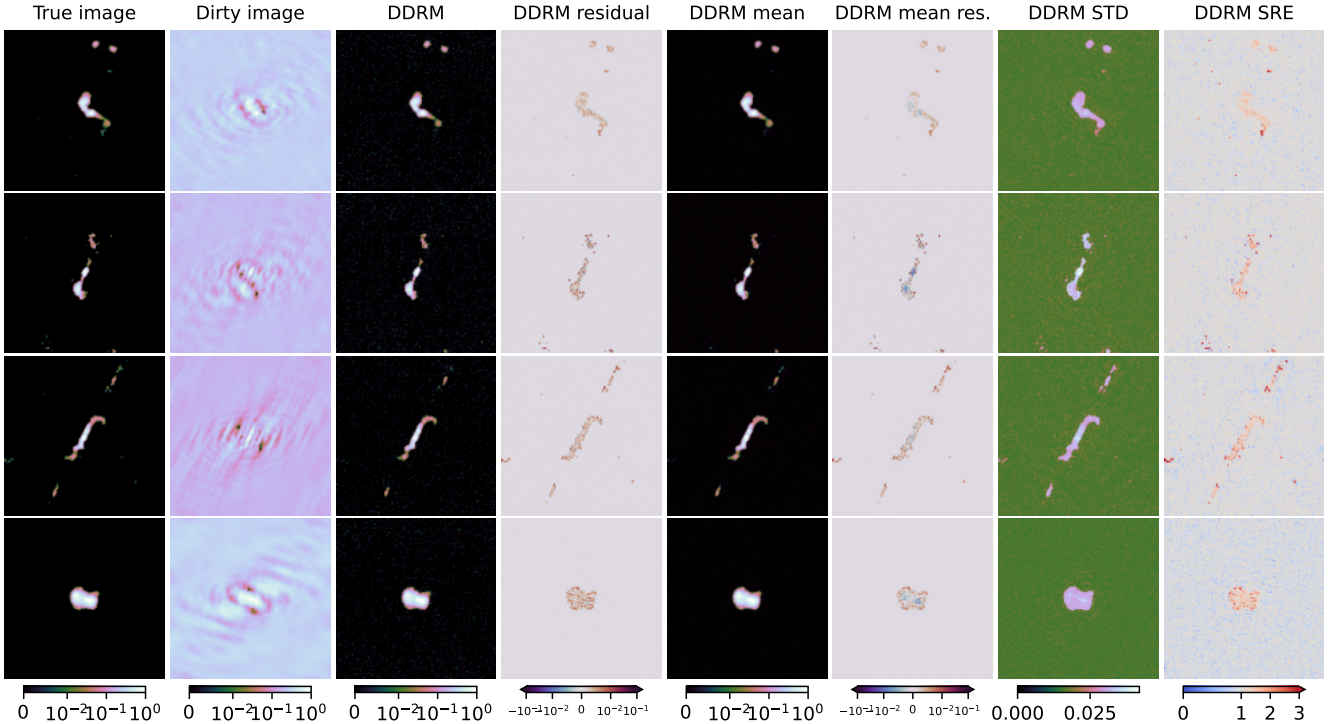


**Figure 4.** DDRM reconstruction results using 1000 sampling steps for four radio galaxies from the test data set using a simulated VLA observation, with no additional noise added. Columns from left to right are: the true image  $\mathbf{x}$ , the dirty image  $\mathbf{x}_D$ , the DDRM restored image, the residual between the DDRM image and the true image, the mean DDRM image, the residual between the mean DDRM image and the true image, the per-pixel standard deviation map, and the SRE. The plots in the last four columns are calculated across 128 DDRM reconstructions. The true and dirty images are scaled to the range  $[0,1]$ , and the flux does not correspond to physical units. All log scale colors revert to linear scale in the range  $[0,0.01]$ .

$K$	MSE	PSNR	SNR	SRE	$t_{\text{sampling}}$ (s)
<b>VLA array configuration</b>					
10	$3.2 \times 10^{-5}$	45.0	36.8	1.39	0.44
50	$1.0 \times 10^{-5}$	49.9	41.7	1.548	2.21
100	$6.6 \times 10^{-6}$	51.8	43.7	1.40	4.41
500	$1.0 \times 10^{-6}$	59.8	51.7	1.44	22.03
1000	$5.2 \times 10^{-7}$	62.9	54.7	1.04	45.47
<b>EHT array configuration</b>					
1000	$6.8 \times 10^{-7}$	61.7	53.5	1.11	-
<b>ALMA array configuration</b>					
1000	$5.25 \times 10^{-7}$	62.8	54.6	1.14	-

**Table 1.** MSE, PSNR, SNR, SRE, and the sampling time  $t_{\text{sampling}}$  as a function of number of sampling steps  $K$ . For every  $K$  the batch size is 128. We note that 99% of the pixels in the ground truth image have very small flux values, below 5% of the maximum value.

DDRM will occasionally miss low-flux components of the images in the reconstruction. However, these low-flux components often appear in the standard deviation map of the DDRM reconstructions, indicating that DDRM is occasionally able to recover these components.

### 3.1 Sampling steps & reconstruction quality

We evaluate the image reconstruction results for different numbers of sampling steps of the DDRM algorithm. Here, the number of sampling steps refers to the number of discrete iterations used during

the reverse procedure. Sampling with  $K$  timesteps where  $K < T$  means selecting  $K$  timesteps of our complete diffusion schedule  $\beta$ . Sampling with a larger number of steps should yield better results at the cost of more time, while using fewer timesteps would trade quality for sampling time. We also evaluate the time to process the sampling steps, calculated using one NVIDIA GH200 GPU on the CSCS Alps infrastructure.

The results are shown in Table 1. We find that MSE improves with higher values of  $K$ , whereas SRE does not depend as strongly on the number of sampling steps. The best MSE of  $5.2 \times 10^{-7}$  is achieved with the maximum sampling steps  $T = 1000$ . However, an excellent MSE of  $3.2 \times 10^{-5}$  is achieved with only 10 sampling steps, which can run in 0.44s, demonstrating the efficiency of DDRM. However, we find that when reducing the number of sample steps, DDRM is less likely to recover faint image components. In the subsequent results, all DDRM reconstructions are run for 1000 sampling steps.

### 3.2 Uncertainty estimation

DDPMs are often used to quantify and model uncertainty in various applications because of their inherent ability to learn the entire data distribution and therefore generate diverse, realistic samples that capture a range of possible outcomes. We evaluate how well the DDPM prior can accurately represent the reconstruction error through the SRE, which measures the reconstruction error relative to the variation in the reconstructions. A well-calibrated network should have  $\text{SRE} \leq 1$ .

We show the standard deviation of 128 reconstructions and the SRE in the two leftmost columns of Figure 4. We find that overall

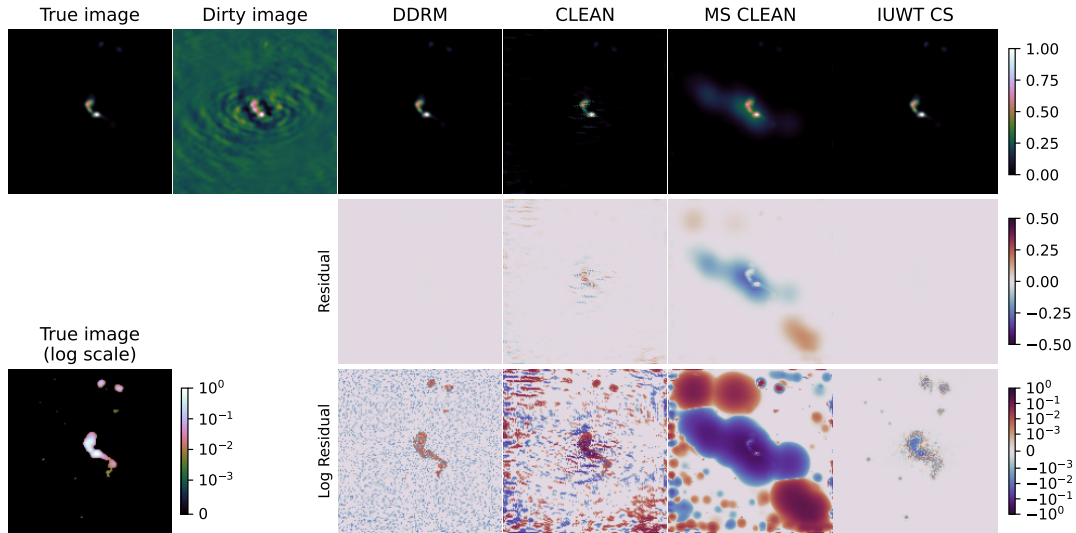


**Figure 5.** Reconstruction results for a radio galaxy from the test data set using a simulated VLA observation, with no additional noise added. Columns from left to right are: the true image  $\mathbf{x}$ , the dirty image  $\mathbf{x}_D$ , the DDRM restored image and its residuals, and then the CLEAN, multi-scale CLEAN, and IUWT compressed sensing reconstructions implemented with the Radler library. The Radler reconstructions are calculated for 100,000 iterations with a major loop gain of 1.0 and a threshold of 0Jy. The true and dirty images are scaled to the range  $[0, 1]$ , and the flux does not correspond to physical units. All log scale colors revert to linear scale in the range  $[-0.001, 0.001]$ .

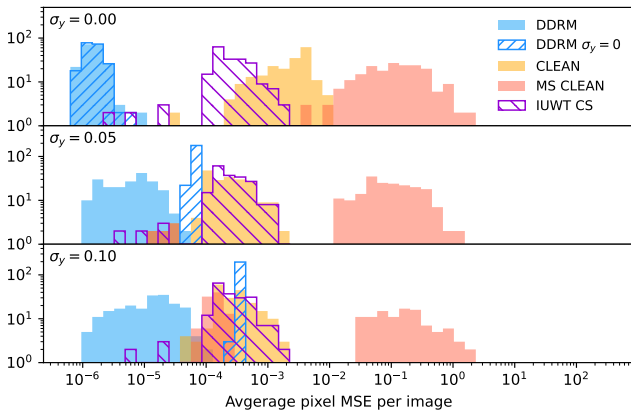


**Figure 6.** Average MSE per image for 200 reconstructed images of the test data set. Reconstruction is done from a simulated VLA observation with noise from  $\sigma_y = 0$  to 0.1. The DDRM restored image uses the true value of  $\sigma_y$  (solid blue), or uses  $\sigma_y = 0$  regardless of the true noise level (diagonal hashed blue). The CLEAN, multi-scale CLEAN, and IUWT compressed sensing reconstructions are calculated for 100,000 iterations with a major loop gain of 1.0 and an “auto threshold” of  $\sigma = 2$ .

the DDRM is overconfident, with values of up to  $\text{SRE} = 8$  where the DDRM image reconstruction has failed to recover low-flux components of the target image. This result is not surprising, as DDPMs are by default uncalibrated (Pang et al. 2023), ie variations in model outputs are smaller than the residuals. The range of DDRM predictions do not accurately represented the reconstruction error, and therefore cannot be used as an image uncertainty. Section 4 presents a discussion of possible improvements and calibration methods.

### 3.3 Comparison to other deconvolution algorithms

We also compare the DDRM restoration results using three other deconvolution algorithms implemented in the Radler: Radio Astronom-

ical Deconvolution Library<sup>1</sup>, which is a module of WSCLEAN (Offringa et al. 2014; Offringa & Smirnov 2017; Van der Tol et al. 2018). We compare the DDRM restoration to “generic” CLEAN, multi-scale (MS) CLEAN, and isotropic undecimated wavelet transform (IUWT) compressed sensing (Dabbech et al. 2015). When performing the reconstruction on the data with zero noise added, we run these Radler reconstructions for 100,000 iterations with a major loop gain of 1.0 and a threshold of 0Jy. When we add noise to the observation, we use automatic thresholding with  $\sigma = 2$  instead of an absolute threshold.

Image reconstruction results for these three algorithms and DDRM reconstruction are shown in Figure 5 for a radio galaxy in the test dataset, with no noise added to the simulated observation. Unlike the CLEAN algorithms, the DDRM reconstruction does not contain any residual dirty beam artifacts. By eye, the DDRM reconstruction looks comparable to the IUWT reconstruction.

We also evaluated the reconstruction quality when including noise in the simulated observations. The the average MSE across all images for the different reconstruction methods are shown in Figure 6. We find that for all tests the DDRM image MSE is at least 2 orders of magnitude smaller than CLEAN, MS CLEAN, and IUWT CS, even in the case of extremely noisy images with  $\sigma_y = 0.1$  (noise level 10% of maximum pixel value).

### 3.4 Incorrect noise and out-of-domain tests

We also explore running the DDRM sampling with an incorrect estimate of the noise, always using  $\sigma_y = 0$  regardless of the correct observation noise. We note that setting  $\sigma_y = 0$  means that the network will inpaint missing visibilities but will not denoise existing visibilities. Figure 6 shows that even when  $\sigma_y = 0.1$  the reconstruction quality is similar to CLEAN and IUWT CS, demonstrating the robustness of the DDRM reconstruction.

We also test reconstruction on several  $150 \times 150$  pixel cutouts of

<sup>1</sup> <https://radler.readthedocs.io/en/latest/index.html>

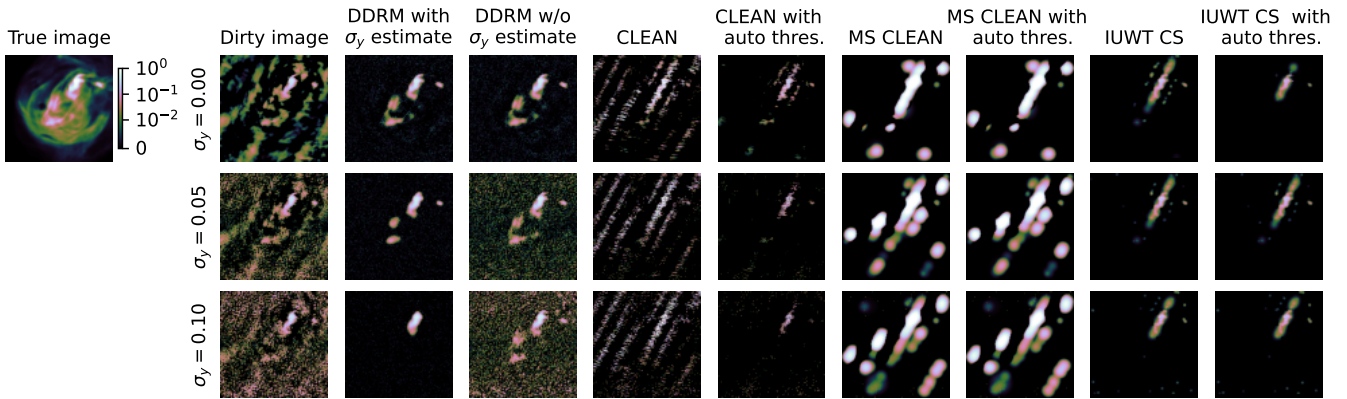


**Figure 7.** Reconstruction results for a  $150 \times 150$  pixel cutout of 3c353, an out-of-domain radio galaxy, imaged from a simulated VLA observation, variable observation noise added from  $\sigma_y = 0$  to 0.1. Columns from left to right are: the true image  $\mathbf{x}$ , the dirty image  $\mathbf{x}_D$ , the DDRM restored image using the true value of  $\sigma_y$ , the DDRM restored image using  $\sigma_y = 0$ , and then the CLEAN, multi-scale CLEAN, and IUWT compressed sensing reconstructions implemented with the Radler library. The Radler reconstructions are calculated for 100,000 iterations with a major loop gain of 1.0. The “auto threshold” columns are imaged using auto thresholding with  $\sigma = 2$ , and the other columns are imaged with a threshold of 0Jy. The true and dirty images are scaled to the range  $[0,1]$ , and the flux does not correspond to physical units. All log scale colors revert to linear scale in the range  $[0,0.01]$ .

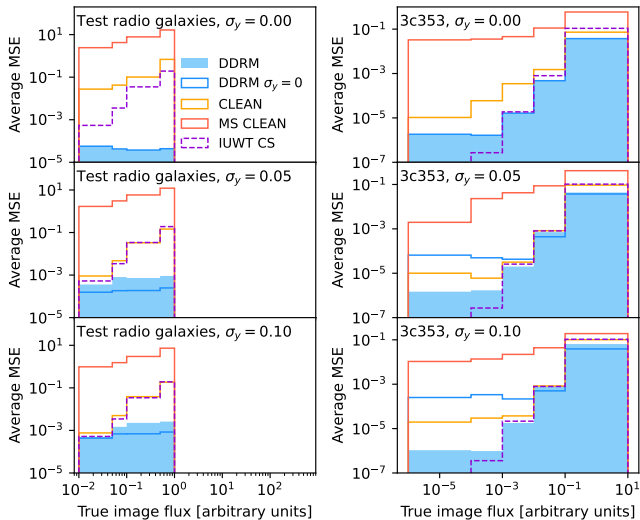


**Figure 8.** MSE as a function of true image pixel brightness for (left) 200 images of the test data set and (right) several different  $150 \times 150$  pixel cutouts of 3c353 and. Reconstruction is done from a simulated VLA observation with noise from  $\sigma_y = 0$  to 0.1. The DDRM restored image uses the true value of  $\sigma_y$  (solid blue), or uses  $\sigma_y = 0$  regardless of the true noise level (dashed blue line). The CLEAN, multi-scale CLEAN, and IUWT compressed sensing reconstructions are calculated for 100,000 iterations with a major loop gain of 1.0 and an “auto threshold” of  $\sigma = 2$ .

the radio galaxy 3c535 which was used as an imaging benchmark in Terris et al. (2023). This image has a much larger dynamic range than our training set, exhibits compact morphology and extended diffuse structures. The radio galaxy and the corresponding reconstruction results are shown in Figure 7. By eye it seems that DDRM is better able to reconstruct the low-flux diffuse components of the image. Columns 2 and 3 show the reconstruction results when running DDRM with the true value of  $\sigma_y$  vs always using  $\sigma_y = 0$ . When DDRM sampling is run without the measurement noise estimate, it is better able to reconstruct the diffuse components of the true image, though the image overall is noisier. The  $\sigma_y$  parameter is used to balance sampling with the prior vs the measurement, so setting

$\sigma_y = 0$  means that the network will only use its low-dynamic range prior when inpainting missing visibilities.

The reconstruction MSE vs true image pixel intensity is shown in Figure 8. Again we see that DDRM outperforms the CLEAN image reconstructions, especially in brighter regions of the image. While DDRM is better at bright pixel values, but IUWT CS is better at low flux values, likely because of its sparsity prior, whereas DDRM images often have some residual noise from the sampling process.

## 4 DISCUSSION & CONCLUSIONS

In this work, we present a new approach to radio interferometric image reconstruction using DDRMs. Our approach naturally incorporates the physics of the measurement process and the noise model. Unlike sparsity-based deconvolution algorithms, DDRM uses a data-driven prior trained on representative data. Unlike other machine learning approaches, DDRM does not need to be trained on the specific array layout.

We find that the DDRM algorithm can propose a range of plausible restorations for the sub-sampled images typically recovered in radio interferometry. The method is less dependent than the CLEAN algorithm on user input, and we also find that images are reconstructed with better MSE compared to CLEAN, MS CLEAN, or IUWT CS. We note that we do not perform any hyperparameter optimization, and the performance could be improved by searching over different network architectures, learning rate schedules, or the  $\eta$  hyperparameters of DDRM.

We use a DDPM prior trained exclusively on VLA images. We do see that the performance of DDRM is best on the test VLA dataset, but we test on one out-of-domain galaxy 3c353 and find that the performance is still better than MS CLEAN and comparable to IUWT CS. We note that the DDRM method can easily be used with a different DDPM such as the one developed by Vičánek Martínez et al. (2024) trained on the LOFAR Two-Metre Sky Survey (LoTSS; Shimwell et al. 2022) or the one developed by Potevineau et al. (2026) trained on MeerKAT data.

Despite the impressive accuracy of the DDRM reconstruction, there are several limitations:

**Image size:** An inherent constraint of the DDRM reconstruction

method is the image size, limited to  $150 \times 150$  pixel images, unlike CLEAN which can be run of images of any size. We are limited to this image size by the available training data of our DDPM. Simulated radio continuum survey maps such as (Vičánek Martínez et al. 2025) could provide larger image sizes to serve as a basis for training.

**Uncertainty:** We did not find that the range of DDRM predictions accurately represented the reconstruction error, and therefore cannot be used as an image uncertainty. This could be improved by calibrating the DDPM (Pang et al. 2023). Recent work by (Teneggi et al. 2023) has shown that conformal prediction can give finite-sample, distribution-free uncertainties for diffusion models. This method allows calibration of uncertainty thresholds on held-out data.

**Transformation operator:** DDRM relies on finding the SVD of the linear transformation operator  $\mathbf{H}$ . In this work we considered a relatively simple transformation consisting of a 2D Fourier transform and  $(u, v)$  sampling. However, contemporary imaging techniques used in radio interferometry need to account for  $A$ -terms  $W$ -terms (Bhatnagar et al. 2008; Cornwell et al. 2008), related to the direction-dependent antenna response and sky curvature, respectively.  $A$ -terms could be accounted for by including a matrix operator representing multiplication of the sky brightness by the primary beam  $\mathbf{A}$ :

$$\mathbf{y} = \mathbf{SFA} \mathbf{x}, \quad (21)$$

extending Equation 3, though a new memory-efficient SVD would need to be defined for this operator.  $W$ -terms can be modeled using the non-uniform discrete Fourier transform (NUDFT; Bagchi & Mitra 1999), but we find that the SVD decomposition is intractably large for realistic observations due to the large number of visibility points.

Another way to use nonlinear transformation operators could be to use Diffusion Posterior Sampling (Chung et al. 2023), where update uses the full nonlinear degradation operator  $H^T(y - Hx)$ .

Any inaccuracies in the transformation operator arising from calibration mismatch would degrade the performance of DDRM. If the transformation operator is inaccurate, the DDRM reconstruction method can be weighted to use more contributions from the DDPM prior by tuning the  $\eta_b$  hyperparameter, though this may degrade performance of out-of-domain sources.

## ACKNOWLEDGMENTS

ET acknowledges financial support from the SNSF under the Starting Grant project Deep Waves (218396). RP acknowledges financial support from the SNSF under the Weave/Lead Agency project Radio-Clusters (214815). This work was supported by the Swiss National Supercomputing Centre (CSCS) under project ID sk031, done in partnership with the SKACH consortium through funding by SERI.

## DATA AVAILABILITY

Details on the FIRST and MiraBest datasets which we used for training are available in Griese et al. (2023) and (Porter & Scaife 2023). The code for training and inference of the model is available at <https://github.com/epfl-radio-astro/diffusionRI.git>

## REFERENCES

Ables, J. G., 1974. Maximum Entropy Spectral Analysis, *A&AS*, **15**, 383.

- Aghabiglou, A., Chu, C. S., Dabbech, A., & Wiaux, Y., 2024. The R2D2 Deep Neural Network Series Paradigm for Fast Precision Imaging in Radio Astronomy, *The Astrophysical Journal Supplement Series*, **273**(1), 3.
- Bagchi, S. & Mitra, S. K., 1999. *The Nonuniform Discrete Fourier Transform and Its Applications in Signal Processing*, The Springer International Series in Engineering and Computer Science, Springer, New York, NY, 1st edn.
- Becker, R. H., White, R. L., & Helfand, D. J., 1995. The first survey: faint images of the radio sky at twenty centimeters, *Astrophysical Journal* v. 450, p. 559, **450**, 559.
- Bergeaud, F. & Mallat, S., 1995. Matching pursuit of images, in *Proceedings, International Conference on Image Processing*, vol. 1, pp. 53–56 vol.1.
- Bhatnagar, S., Cornwell, T. J., Golap, K., & Uson, J. M., 2008. Correcting direction-dependent gains in the deconvolution of radio interferometric images, *Astronomy & Astrophysics*, **487**(1), 419–429.
- Carrillo, R. E., McEwen, J. D., & Wiaux, Y., 2012. Sparsity averaging reweighted analysis (sara): a novel algorithm for radio-interferometric imaging: Sara for radio-interferometric imaging, *Monthly Notices of the Royal Astronomical Society*, **426**(2), 1223–1234.
- Chung, H., Kim, J., Mccann, M. T., Klasky, M. L., & Ye, J. C., 2023. Diffusion posterior sampling for general noisy inverse problems, in *The Eleventh International Conference on Learning Representations*.
- Connor, L., Bouman, K. L., Ravi, V., & Hallinan, G., 2022. Deep radio-interferometric imaging with POLISH: DSA-2000 and weak lensing, *MNRAS*, **514**(2), 2614–2626.
- Cornwell, T. J., 2008. Multiscale clean deconvolution of radio synthesis images, *IEEE Journal of Selected Topics in Signal Processing*, **2**(5), 793–801.
- Cornwell, T. J. & Evans, K. F., 1985. A simple maximum entropy deconvolution algorithm, *A&A*, **143**(1), 77–83.
- Cornwell, T. J. & Perley, R. A., 1992. Radio-interferometric imaging of very large fields. The problem of non-coplanar arrays., *A&A*, **261**, 353–364.
- Cornwell, T. J., Golap, K., & Bhatnagar, S., 2008. The noncoplanar baselines effect in radio interferometry: The w-projection algorithm, *IEEE Journal of Selected Topics in Signal Processing*, **2**(5), 647–657.
- Dabbech, A., Ferrari, C., Mary, D., Slezak, E., Smirnov, O., & Kenyon, J. S., 2015. MORESANE: MOdel REconstruction by Synthesis-ANalysis Estimators. A sparse deconvolution algorithm for radio interferometric imaging, *A&A*, **576**, A7.
- Drozдова, M., Kinakh, V., Bait, O., Taran, O., Lastufka, E., Dessauges-Zavadsky, M., Holotyak, T., Schaerer, D., & Voloshynovskiy, S., 2024. Radio-astronomical image reconstruction with a conditional denoising diffusion model, *A&A*, **683**, A105.
- Event Horizon Telescope Collaboration, 2019. First M87 Event Horizon Telescope Results. II. Array and Instrumentation, *ApJ*, **875**(1), L2.
- Gheller, C. & Vazza, F., 2022. Convolutional deep denoising autoencoders for radio astronomical images, *MNRAS*, **509**(1), 990–1009.
- Griese, F., Kummer, J., Connor, P., Brüggem, M., & Rustige, L., 2023. First radio galaxy data set containing curated labels of classes fri, frii, compact and bent, *Data in Brief*, **47**, 108974.
- He, K., Zhang, X., Ren, S., & Sun, J., 2016. Deep Residual Learning for Image Recognition, in *2016 IEEE Conference on Computer Vision and Pattern Recognition (CVPR)*, p. 1.
- He, K., Zhang, X., Ren, S., & Sun, J., 2016. Deep residual learning for image recognition, in *2016 IEEE Conference on Computer Vision and Pattern Recognition (CVPR)*, pp. 770–778.
- Ho, J., Jain, A., & Abbeel, P., 2020. Denoising diffusion probabilistic models.
- Högbom, J. A., 1974. Aperture Synthesis with a Non-Regular Distribution of Interferometer Baselines, *A&AS*, **15**, 417.
- Kawar, B., Elad, M., Ermon, S., & Song, J., 2022. Denoising diffusion restoration models, in *Advances in Neural Information Processing Systems*.
- Lei Ba, J., Kiros, J. R., & Hinton, G. E., 2016. Layer Normalization, *arXiv e-prints*, p. arXiv:1607.06450.
- Li, F., Cornwell, T. J., & de Hoog, F., 2011. The application of compressive sampling to radio astronomy. I. Deconvolution, *A&A*, **528**, A31.
- Loshchilov, I. & Hutter, F., 2016. SGDR: Stochastic Gradient Descent with Warm Restarts, *arXiv e-prints*, p. arXiv:1608.03983.
- Loshchilov, I. & Hutter, F., 2017. Decoupled Weight Decay Regularization,

- arXiv e-prints*, p. arXiv:1711.05101.
- Narayan, R. & Nityananda, R., 1986. Maximum entropy image restoration in astronomy., *ARA&A*, **24**, 127–170.
- Offringa, A. R. & Smirnov, O., 2017. An optimized algorithm for multiscale wideband deconvolution of radio astronomical images, *MNRAS*, **471**(1), 301–316.
- Offringa, A. R., McKinley, B., Hurley-Walker, et al., 2014. WSClean: an implementation of a fast, generic wide-field imager for radio astronomy, *MNRAS*, **444**(1), 606–619.
- Ord, S. M., Mitchell, D. A., Wayth, R. B., Greenhill, L. J., Bernardi, G., Gleadow, S., Edgar, R. G., Clark, M. A., Allen, G., Arcus, W., Benkevitch, L., Bowman, J. D., Briggs, F. H., Bunton, J. D., Burns, S., Cappallo, R. J., Coles, W. A., Corey, B. E., deSouza, L., Doeleman, S. S., Derome, M., Deshpande, A., Emrich, D., Goeke, R., Gopalakrishna, M. R., Herne, D., Hewitt, J. N., Kamini, P. A., Kaplan, D. L., Kasper, J. C., Kincaid, B. B., Kocz, J., Kowald, E., Kratzenberg, E., Kumar, D., Lonsdale, C. J., Lynch, M. J., McWhirter, S. R., Madhavi, S., Matejek, M., Morales, M. F., Morgan, E., Oberoi, D., Pathikulangara, J., Prabu, T., Rogers, A. E. E., Roshii, A., Salah, J. E., Schinkel, A., Udaya Shankar, N., Srivani, K. S., Stevens, J., Tingay, S. J., Vaccarella, A., Waterson, M., Webster, R. L., Whitney, A. R., Williams, A., & Williams, C., 2010. Interferometric imaging with the 32 element Murchison wide-field array, *Publications of the Astronomical Society of the Pacific*, **122**(897), 1353–1366.
- Ostrovsky, A. S., Martínez-Niconoff, G., Martínez-Vara, P., & Olvera-Santamaría, M. A., 2009. The van Cittert-Zernike theorem for electromagnetic fields, *Optics Express*, **17**(3), 1746.
- Pang, T., Lu, C., Du, C., Lin, M., YAN, S., & Deng, Z., 2023. On calibrating diffusion probabilistic models, in *Thirty-seventh Conference on Neural Information Processing Systems*.
- Perez, E., Strub, F., de Vries, H., Dumoulin, V., & Courville, A., 2017. FiLM: Visual Reasoning with a General Conditioning Layer, *arXiv e-prints*, p. arXiv:1709.07871.
- Ponsonby, J. E. B., 1973. An entropy measure for partially polarized radiation and its application to estimating radio sky polarization distributions from incomplete ‘aperture synthesis’ data by the maximum entropy method, *Monthly Notices of the Royal Astronomical Society*, **163**(4), 369–380.
- Porter, F. A. M. & Scaife, A. M. M., 2023. MiraBest: a data set of morphologically classified radio galaxies for machine learning, *RAS Techniques and Instruments*, **2**(1), 293–306.
- Potevineau, R., Tolley, E., & Etsebeth, V., 2026. A Guided Unconditional Diffusion Model to Synthesize and Inpaint Radio Galaxies from FIRST, MGCLS and Radio Zoo, *arXiv e-prints*, p. arXiv:2601.07485.
- Rich, J. W., de Blok, W. J. G., Cornwell, T. J., Brinks, E., Walter, F., Bagetakos, I., & Kennicutt, Jr., R. C., 2008. Multi-Scale CLEAN: A Comparison of its Performance Against Classical CLEAN on Galaxies Using THINGS, *AJ*, **136**(6), 2897–2920.
- Ronneberger, O., Fischer, P., & Brox, T., 2015. U-Net: Convolutional Neural Networks for Biomedical Image Segmentation, *arXiv e-prints*, p. arXiv:1505.04597.
- Schmidt, K., Geyer, F., Fröse, S., Blomenkamp, P.-S., Brügger, M., de Gasperin, F., Elsässer, D., & Rhode, W., 2022. Deep learning-based imaging in radio interferometry, *A&A*, **664**, A134.
- Shimwell, T. W., Hardcastle, M. J., Tasse, C., Best, P. N., Röttgering, H. J. A., Williams, W. L., Botteon, A., Drabent, A., Mechev, A., Shulevski, A., van Weeren, R. J., Bester, L., Brügger, M., Brunetti, G., Callingham, J. R., Chyży, K. T., Conway, J. E., Dijkema, T. J., Duncan, K., de Gasperin, F., Hale, C. L., Haverkorn, M., Hugo, B., Jackson, N., Mevius, M., Miley, G. K., Morabito, L. K., Morganti, R., Offringa, A., Oonk, J. B. R., Rafferty, D., Sabater, J., Smith, D. J. B., Schwarz, D. J., Smirnov, O., O’Sullivan, S. P., Vedantham, H., White, G. J., Albert, J. G., Alegre, L., Asabere, B., Bacon, D. J., Bonafede, A., Bonnassieux, E., Brienza, M., Bilicki, M., Bonato, M., Calistro Rivera, G., Cassano, R., Cochrane, R., Croston, J. H., Cuciti, V., Dallacasa, D., Danezi, A., Dettmar, R. J., Di Gennaro, G., Edler, H. W., Enßlin, T. A., Emig, K. L., Franzen, T. M. O., García-Vergara, C., Grange, Y. G., Gürkan, G., Hajduk, M., Heald, G., Heesen, V., Hoang, D. N., Hoefl, M., Horellou, C., Iacobelli, M., Jamroz, M., Jelić, V., Kondapally, R., Kukreti, P., Kunert-Bajraszewska, M., Magliocchetti, M., Mahatma, V., Mafek, K., Mandal, S., Massaro, F., Meyer-Zhao, Z., Mingo, B., Mostert, R. I. J., Nair, D. G., Nakoneczny, S. J., Nikiel-Wroczyński, B., Orrú, E., Pajdosz-Śmierciak, U., Pasini, T., Prandoni, I., van Piggelen, H. E., Rajpurohit, K., Retana-Montenegro, E., Riseley, C. J., Rowlinson, A., Saxena, A., Schrijvers, C., Sweijen, F., Siewert, T. M., Timmerman, R., Vaccari, M., Vink, J., West, J. L., Wołowska, A., Zhang, X., & Zheng, J., 2022. The LOFAR Two-metre Sky Survey. V. Second data release, *A&A*, **659**, A1.
- Starck, J.-L., Fadili, J., & Murtagh, F., 2007. The Undecimated Wavelet Decomposition and its Reconstruction, *IEEE Transactions on Image Processing*, **16**(2), 297–309.
- Taran, O., Bait, O., Dessauges-Zavadsky, M., Holotyak, T., Schaerer, D., & Voloshynovskiy, S., 2023. Challenging interferometric imaging: Machine learning-based source localization from uv-plane observations, *A&A*, **674**, A161.
- Teneggi, J., Tivnan, M., Webster Stayman, J., & Sulam, J., 2023. How to Trust Your Diffusion Model: A Convex Optimization Approach to Conformal Risk Control, *arXiv e-prints*, p. arXiv:2302.03791.
- Terris, M., Dabbech, A., Tang, C., & Wiaux, Y., 2023. Image reconstruction algorithms in radio interferometry: From handcrafted to learned regularization denoisers, *MNRAS*, **518**(1), 604–622.
- The Event Horizon Telescope Collaboration, 2019. First m87 event horizon telescope results. iv. imaging the central supermassive black hole, *The Astrophysical Journal Letters*, **875**(1), L4.
- Thyagarajan, N., Beardsley, A. P., Bowman, J. D., & Morales, M. F., 2017. A generic and efficient e-field parallel imaging correlator for next-generation radio telescopes, *Monthly Notices of the Royal Astronomical Society*, **467**(1), 715–730.
- Van der Tol, S., Veenboer, B., & Offringa, A. R., 2018. Image domain gridding: a fast method for convolutional resampling of visibilities, *A&A*, **616**, A27.
- Vičánek Martínez, T., Baron Perez, N., & Brügger, M., 2024. Simulating images of radio galaxies with diffusion models, *Astronomy and Astrophysics*, **691**, A360.
- Vičánek Martínez, T., Edler, H. W., & Brügger, M., 2025. Simulating realistic radio continuum survey maps with diffusion models, *A&A*, **700**, A18.
- Wang, R., Chen, Z., Luo, Q., & Wang, F., 2023. A conditional denoising diffusion probabilistic model for radio interferometric image reconstruction, in *Proceedings of the 26th European Conference on Artificial Intelligence (ECAI 2023)*, vol. 372 of *Frontiers in Artificial Intelligence and Applications*, pp. 2499–2506, IOS Press.
- Wiaux, Y., Jacques, L., Puy, G., Scaife, A. M. M., & Vanderghenst, P., 2009. Compressed sensing imaging techniques for radio interferometry, *Monthly Notices of the Royal Astronomical Society*, **395**(3), 1733–1742.
- Wong, O. I., Garon, A. F., Alger, M. J., Rudnick, L., Shabala, S. S., Willett, K. W., Banfield, J. K., Andernach, H., Norris, R. P., Swan, J., Hardcastle, M. J., Lintott, C. J., White, S. V., Seymour, N., Kapińska, A. D., Tang, H., Simmons, B. D., & Schawinski, K., 2025. Radio Galaxy Zoo data release 1: 100185 radio source classifications from the FIRST and ATLAS surveys, *MNRAS*, **536**(4), 3488–3506.
- Zawadzki, B., Czekala, I., Loomis, R. A., Quinn, T., Grzybowski, H., Frazier, R. C., Jennings, J., Nizam, K. M., & Jian, Y., 2023. Regularized Maximum Likelihood Image Synthesis and Validation for ALMA Continuum Observations of Protoplanetary Disks, *PASP*, **135**(1048), 064503.

## APPENDIX A: UNIFORM VS NATURAL UV WEIGHTS

The transformation operator considered in throughout the paper corresponds to *uniform* weighting, giving all uv bins the same weight. Different weight schemes are easily implemented with DDRM, and corresponds to modifying the singular values of the operator. We also test *natural* weighting, giving each uv bin a weight proportional to the number of uv samples in the bin. When doing image reconstruction, DDRM will use the observation constraint more strongly in portions of visibility space that have a large weight compared to the observation noise, as discussed in Section 2.3. The results are shown

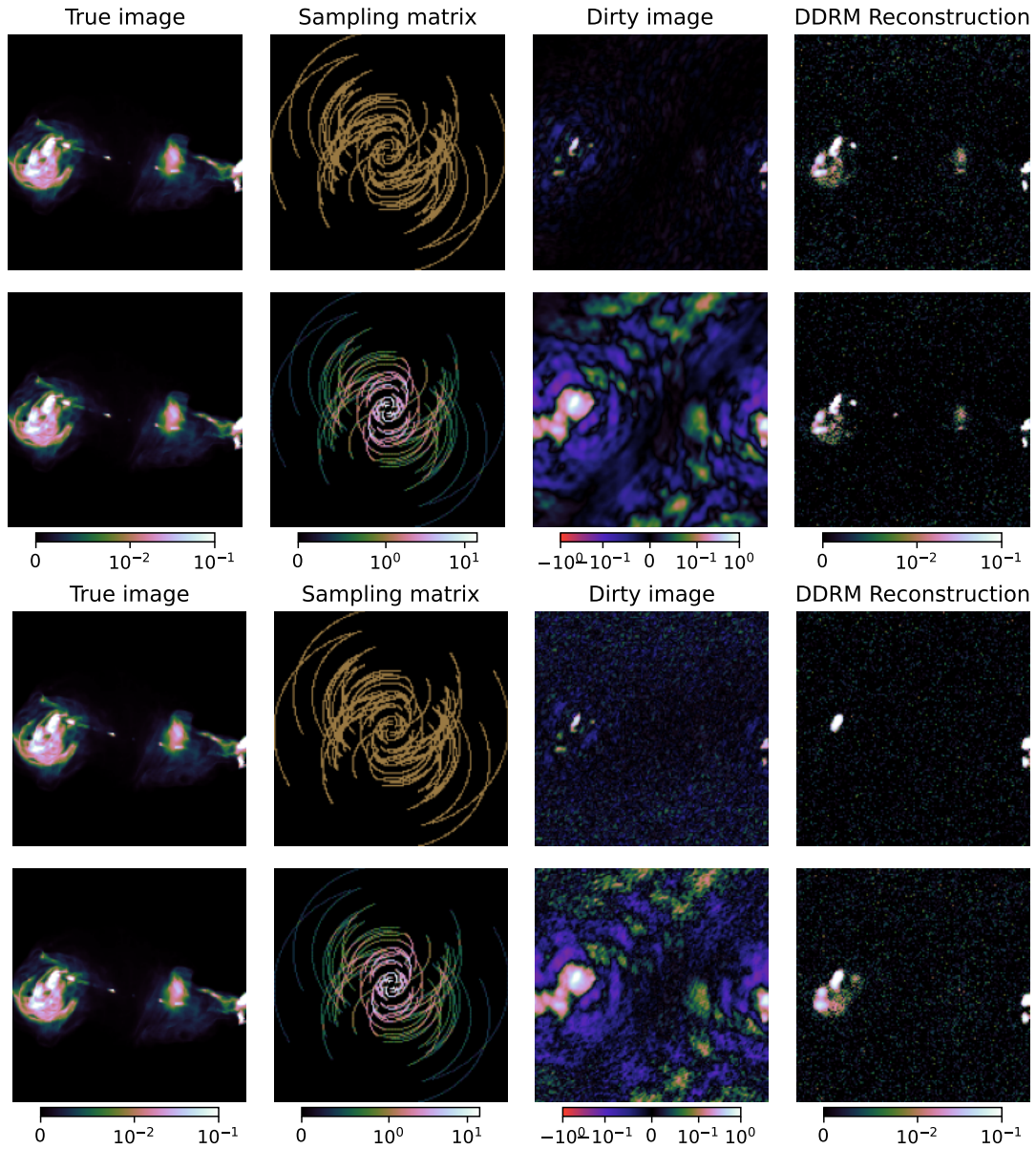


**Figure 1.** Reconstructing a  $150 \times 150$  pixel image of 3c353 using uniform (all uv bins get the same weight) and natural (uv bins are weighted according to the number of uv samples) weighting, with  $\sigma_y = 0$  (top) and  $\sigma_y = 0.05$  (bottom).

in Figure 1. When the observation has no noise (top two rows), the reconstructions are equivalent. When the observation is noisy, DDRM trusts the higher-weight central baselines more, resulting in better reconstruction of large-scale diffuse emission.

This paper has been typeset from a  $\text{\TeX}/\text{\LaTeX}$  file prepared by the author.

## APPENDIX B: ADDITIONAL OUT-OF-DOMAIN IMAGE RECONSTRUCTION TESTS

We test the DDRM reconstruction performance on two additional out-of-domain images, the letter ‘E’ (shown in Figure B1) and a randomly-spaced grid of point sources (shown in Figure B2). With no observation noise  $\sigma_y = 0$ , DDRM only inpaints the missing visibility data using the prior from the DDPM. As  $\sigma_y$  increases, the DDRM denoises the visibilities using the prior.

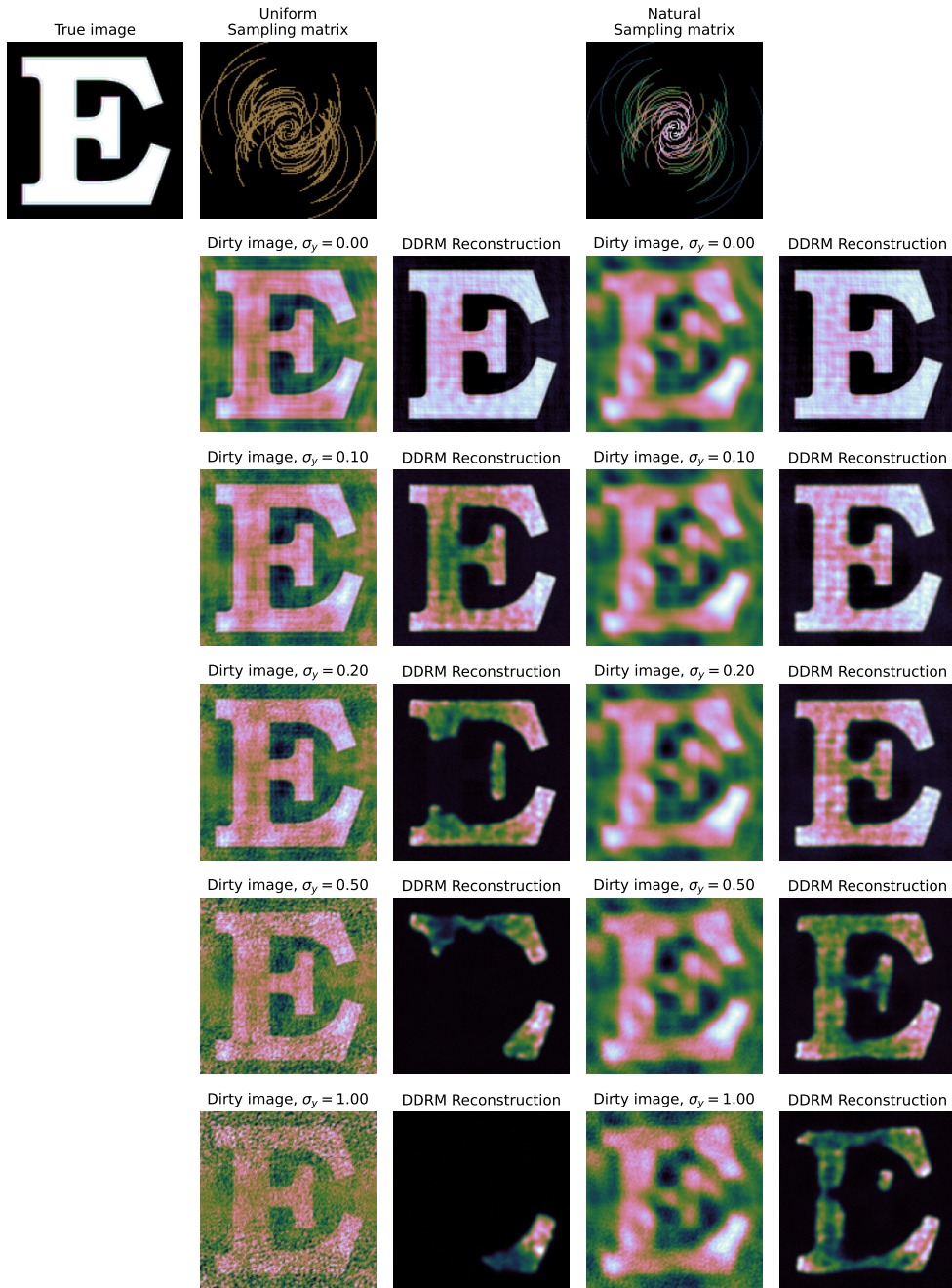


**Figure B1.** Reconstructing a  $150 \times 150$  pixel image using uniform (all uv bins get the same weight) and natural (uv bins are weighted according to the number of uv samples) weighting, going from observation noise of  $\sigma_y = 0$  (top) and  $\sigma_y = 1.0$  (bottom).

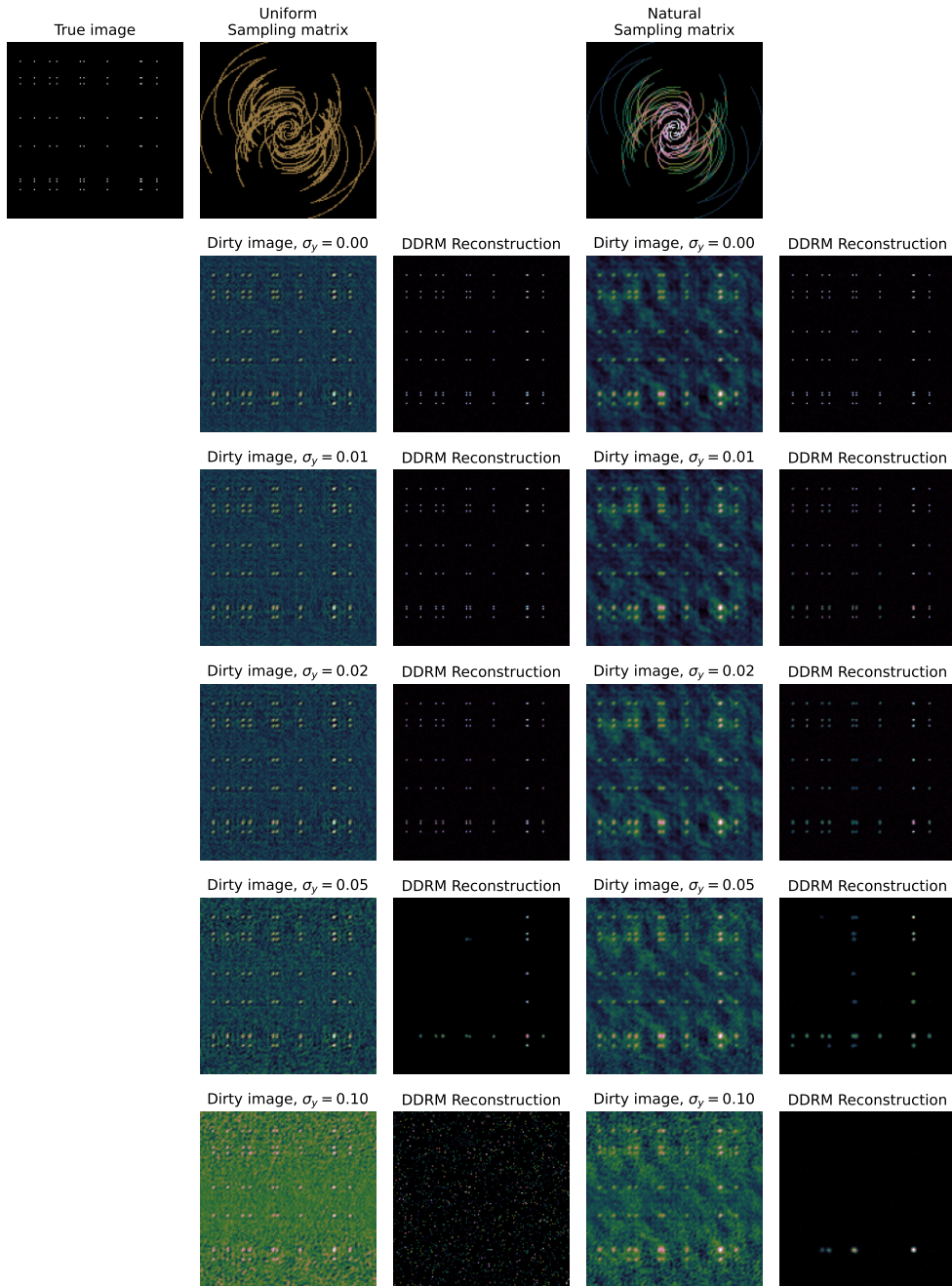


**Figure B2.** Reconstructing a  $150 \times 150$  pixel image of a random grid of single-pixel dots using uniform (all uv bins get the same weight) and natural (uv bins are weighted according to the number of uv samples) weighting, going from observation noise of  $\sigma_y = 0$  (top) and  $\sigma_y = 0.1$  (bottom).